Growing heterogeneous tumors in silico

Jana Gevertz[1,*] and S. Torquato[1,2,3,4,5,†]

[1]*Program in Applied and Computational Mathematics, Princeton University, Princeton, New Jersey 08544, USA*
[2]*Department of Chemistry, Princeton University, Princeton, New Jersey 08544, USA*
[3]*Princeton Center for Theoretical Science, Princeton University, Princeton, New Jersey 08544, USA*
[4]*Princeton Institute for the Science and Technology of Materials, Princeton University, Princeton, New Jersey 08544, USA*
[5]*School of Natural Sciences, Institute for Advanced Study, Princeton, New Jersey 08540, USA*

An *in silico* tool that can be utilized in the clinic to predict neoplastic progression and propose individualized treatment strategies is the holy grail of computational tumor modeling. Building such a tool requires the development and successful integration of a number of biophysical and mathematical models. In this paper, we work toward this long-term goal by formulating a cellular automaton model of tumor growth that accounts for several different inter-tumor processes and host-tumor interactions. In particular, the algorithm couples the remodeling of the microvasculature with the evolution of the tumor mass and considers the impact that organ-imposed physical confinement and environmental heterogeneity have on tumor size and shape. Furthermore, the algorithm is able to account for cell-level heterogeneity, allowing us to explore the likelihood that different advantageous and deleterious mutations survive in the tumor cell population. This computational tool we have built has a number of applications in its current form in both predicting tumor growth and predicting response to treatment. Moreover, the latent power of our algorithm is that it also suggests other tumor-related processes that need to be accounted for and calls for the conduction of new experiments to validate the model's predictions.

I. INTRODUCTION

Cancer is a highly complex and heterogeneous set of diseases. Dynamic changes in the genome, epigenome, transcriptome, and proteome that result in the gain of function of oncoproteins or the loss of function of tumor suppressor proteins underlie the development of all cancers. While the principles that govern the transformation of normal cells into malignant ones are rather well understood [1], having knowledge of these changes has not yet proven sufficient to deduce clinical outcome.

The difficulty in predicting clinical outcome arises because many factors other than the mutations responsible for oncogenesis determine tumor growth dynamics. It has been observed that many complex interactions occur between tumor cells and between a cancer and the host environment. Multidirectional feedback loops occur between tumor cells and the stroma, immune cells, extracellular matrix, and vasculature [2,3]. Given the number and nature of these interactions, it becomes increasingly difficult to reason through the feedback loops and correctly predict tumor behavior.

For these reasons, a better understanding of tumor growth dynamics can be expected from a computational model. The holy grail of computational tumor modeling is to develop a simulation tool that can be utilized in the clinic to predict neoplastic progression and response to treatment. Not only must such a model incorporate the many feedback loops involved in neoplastic progression, the model must also account for the fact that cancer progression involves events occurring over a range of spatial and temporal scales [4]. A successful model would enable one to broaden the conclusions drawn from existing medical data, suggest new experiments, test hypotheses, predict behavior in experimentally unobservable situations, and be employed for early detection.

Over the past several decades, an incredibly large body of research has been developed in the field of biophysical cancer modeling. While an extensive overview of the field is beyond the scope of the text, it is useful to briefly explore both the biological processes that have been incorporated and the computational techniques used to analyze a range of tumor growth models. From a biological perspective, a number of intertumor processes and host-tumor interactions have been studied via modeling. These include, but are not limited to, the impact of different sequences of genetic mutations on tumor emergence and survival [5,6], the competition for spaces and resources between cells (both normal and malignant) [4,7], the interactions between the tumor and the host immune system [8,9], and the remodeling of the host blood supply or extracellular matrix by a growing tumor [10–15].

A range of theoretical techniques have been brought to bear on these biological problems. Macroscopic phenomena (such as the evolution of tumor cell concentration and nutrient concentration) are typically modeled using coupled partial differential equations that are either diffusion based or developed in the realm of continuum and fluid mechanics [15–19]. Mesoscopic phenomena, including but not limited to cell-level dynamics (growth and invasion) and angiogenesis, draw on both deterministic [9,20] and stochastic modeling approaches [6,14,21,22]. At the microscopic scale much emphasis has been placed on quantitatively studying the interactions between molecular species within subcellular compartments. Both deterministic approaches (typically

---

*Present address: Department of Mathematics and Statistics, The College of New Jersey, Ewing, New Jersey 08628, USA
†torquato@princeton.edu

based on mass-action kinetic principles [15,23–25]) and sto-chastic approaches [26] have been utilized to model micro-scopic contributions to tumor growth.

In the current paper, we seek to build upon the set of biophysical tools available to predict tumor growth in heterogeneous and vascular environments. This algorithm merges, adapts, and improves upon the following models of tumor growth that were previously developed by our group: (1) original cellular automaton (CA) model of three-dimensional (3D) tumor growth [21]; (2) vasculature evolution model that explores the feedback between a growing neoplasm and the host blood vessel network [14]; (3) environmentally con-strained growth algorithm that considers the impact that organ-imposed physical confinement and environmental het-erogeneity have on tumor growth [27]; (4) heterogeneous cell population model in which genetic mutations can alter a tumor cell's phenotype [28,29].

The result of merging and expanding upon these models is a versatile, more comprehensive cancer simulation tool with potential clinical applications. For example, as we will ex-plore in Sec. V, the model can be used to determine some necessary features to include in a clinically relevant cancer simulation tool and it can be used to test the effect that dif-ferent treatment strategies have on tumor progression. Fur-thermore, since the tumor-host interactions considered in the model occur at different length scales (at the cellular level for the mutations and vasculature and at the tissue level for confinement effects), this more comprehensive model also tackles the problem of how to integrate these changes into a single tumor growth algorithm.

In Sec. II, we briefly review the relevant previous tumor models. In Sec. III, we describe how we merge, adapt, and expand these models to obtain a more comprehensive model of tumor growth. In Sec. IV, we apply the algorithm to study various scenarios for tumor growth and present results. Sec-tion V discusses ramifications of the model and conclusions are given in Sec. VI.

II. MODEL BACKGROUND

The algorithm we present here merges and modifies pre-viously developed models of tumor growth that stem from a CA model developed by Kansal *et al.* [21]. In the original CA algorithm, it was shown that three-dimensional tumor growth and composition can be realistically predicted by a simple set of automaton rules and a set of four microscopic parameters that account for the nutritional needs of the tu-mor, cell-doubling time, and an imposed spherical symmetry term [21]. The success of this model is in part related to its simplicity, and one of the simplifying assumptions is that the vasculature is implicitly present and evolves as the tumor grows. In order to incorporate more biological detail into the model, the algorithm has previously been modified to study the feedback that occurs between the growing tumor and the evolving host blood supply [14]. While this modification to the algorithm allows new growth scenarios to be tested and new therapies to be explored, both the modified and original versions of the model limit the effects of mechanical con-finement to one parameter that imposes a maximum radius

on a spherically symmetric tumor. Since tumors can grow in organs of any shape with nonhomogeneous tissue structure, we have also previously generalized the original algorithm to allow growth in any confining heterogeneous environment [27]. However, until now, the vascular-growth and environ-mentally constrained scenarios were treated separately. In or-der to maximize the utility of these models, here we discuss how improved versions of these algorithms can be merged into one simulation tool that can be used to explore more scenarios than any of the previous models in isolation.

A. Vascular network evolution

In order to incorporate a higher level of biological realism into the original CA algorithm, a two-dimensional (2D) hy-brid cellular automaton model was developed to explore the feedback that occurs between a growing tumor and the evolving host blood supply [14]. The computational algo-rithm is based on the co-option-regression-growth experi-mental model of tumor vasculature evolution [30]. In this model, as a malignant mass grows, the tumor cells co-opt the mature vessels of the surrounding tissue that express con-stant levels of bound angiopoietin-1 (Ang-1). Vessel co-option leads to the upregulation of the antagonist of Ang-1, angiopoietin-2 (Ang-2). In the absence of the anti-apoptotic signal triggered by vascular endothelial growth factor (VEGF), this shift destabilizes the co-opted vessels within the tumor center and marks them for regression [30]. Vessel regression in the absence of vessel growth leads to the for-mation of hypoxic regions in the tumor mass. Hypoxia in-duces the expression of VEGF, which in turn stimulates the growth of new blood vessels.

A system of reaction-diffusion equations was developed to track the spatial and temporal evolution of the aforemen-tioned key factors involved in blood vessel growth and re-gression. Based on a set of algorithmic rules, the concentra-tion of each protein and bound receptor at a blood vessel determines if a vessel will divide, regress, or remain stag-nant. The structure of the blood vessel network, in turn, is used to estimate the oxygen concentration at each cell site. Oxygen levels determine the proliferative capacity of each automaton cell. The reader is referred to Ref. [14] for the full details of this algorithm. The model proved to quantitatively agree with experimental observations on the growth of tu-mors when angiogenesis is successfully initiated and when angiogenesis is inhibited. Further, due to the biological de-tails incorporated into the model, the algorithm was used to explore tumor response to a variety of single and multimodal treatment strategies [14].

B. Environmentally constrained growth

An assumption made in both the original CA algorithm and the vascular algorithm is that the tumor is growing in a spherically symmetric fashion. In a study performed by Helmlinger *et al.* [31], it was eloquently demonstrated that neoplastic growth is spherically symmetric only when the environment in which the tumor is developing imposes no physical boundaries on growth. In particular, it was shown that human adenocarcinoma cells grown in a 0.7% gel that is

placed in a cylindrical glass tube develop to take on an ellipsoidal shape, driven by the geometry of the capillary tube. However, when the same cells are grown in the same gel outside the capillary tube, a spherical mass develops [31]. This experiment clearly highlights that the assumption of radially symmetric growth is only valid when a tumor grows in an unconfined or spherically symmetric environment.

Since many organs, including the brain and spinal cord, impose nonradially symmetric physical confinement on tumor growth, we modified the original CA algorithm to incorporate boundary and heterogeneity effects on neoplastic progression [27]. The first modification that has to be made to the original algorithm is simply to define the boundary that is confining tumor growth. More importantly, several modifications have to be made to the original automaton rules to account for the impact of this boundary on neoplastic progression. The original CA algorithm imposed radial symmetry in order to determine whether a cancer cell is proliferative, hypoxic, or necrotic. The assumption of radially symmetric growth was also utilized in determining the probability a proliferative cell divides. In order to permit tumor growth in any confining environment, the algorithm was modified to remove all assumptions of radial symmetry from the automaton evolution rules. In doing this, we showed that models that do not account for the geometry of the confining boundary and the heterogeneity in tissue structure lead to inaccurate predictions on tumor size, shape, and spread (the distribution of cells throughout the growth-permitting region) [27].

C. Genetic mutations

While there are many benefits to merging the previously described algorithms, one feature that the merged model (as described thus far) does not address is that each patient's tumor has its own genetic profile and that this profile is important in determining growth dynamics and response to treatment. This is a well-established biological fact that we have previously treated theoretically. In particular, in Ref. [28] it was shown that mutant populations which confer no growth rate advantage can emerge in the tumor mass and that the emergence of any mutant strain can drastically alter tumor growth dynamics. The influence that just one mutant strain can have on prognosis was shown to be significant suggesting that our merged algorithm can benefit greatly by accounting for tumor cell heterogeneity.

III. METHODS

Each of the previously discussed algorithms were designed to answer a particular set of questions and successfully served their purpose. It is therefore very useful to merge each algorithm into a single cancer simulation tool that cannot only accomplish what each individual algorithm accomplishes, but can also be expected to have emergent properties not identifiable prior to model integration.

A. Vascular network evolution in confined environments

In this section, we will outline the merged cancer simulation tool. For more details on implementing the vascular evolution aspects of the model, the reader is referred to Ref. [14]. For more details on implementing tumor growth in confined regions, the reader is referred to Ref. [27]. In developing the merged algorithm, some modifications were made to the automaton rules to more realistically mimic tumor progression. The modifications incorporated in the simulation tool will also be highlighted here.

(1) Automaton cell generation: a Voronoi tessellation of random points generated using the nonequilibrium procedure of random sequential addition of hard disks determines the underlying lattice for our algorithm [21,32]. Each automaton cell created via this procedure represents a cluster of biological cells.

(2) Define confining boundary: each automaton cell is divided into one of two regimes—nonmalignant cells within the confining boundary and nonmalignant cells outside of the boundary.

(3) Healthy microvascular network: the blood vessel network which supplies the cells in the tissue region of interest with oxygen and nutrients is generated using the random analog of the Krogh cylinder model detailed in Ref. [14]. One aspect of the merger involved limiting blood vessel development to the subset of space in which tumor growth occurs.

(4) Initialize tumor: designate a chosen nonmalignant cell inside the growth-permitting environment as a proliferative cancer cell.

(5) Tumor growth algorithm: time is then discretized into units that represent one real day. At each time step:

(a) Solve partial differential equations: a previously developed system of partial differential equations [14] is numerically solved one day forward in time. The quantities that govern vasculature evolution, and hence are included in the equations, are concentrations of VEGF (v), unoccupied VEGFR-2 receptors (r_{v0}), the VEGFR-2 receptor occupied with VEGF (r_v), Ang-1 (a_1), Ang-2 (a_2), the unoccupied angiopoietin receptor Tie-2 (r_{a0}), the Tie-2 receptor occupied with Ang-1 (r_{a1}), and the Tie-2 receptor occupied with Ang-2 (r_{a2}). The parameters in these equations include diffusion coefficients of protein x (D_x), production rates b_x and $\bar{b}_x$, carrying capacities K_x, association and dissociation rates ligand-receptor complex y (k_y and k_{-y}), and decay rates μ_x. Any term with a subscript i denotes an indicator function; for example, p_i is a proliferative cell indicator function. It equals 1 if a proliferative cell is present in a particular region of space, and it equals 0 otherwise. Likewise, h_i is the hypoxic cell indicator function, n_i is the necrotic cell indicator function, and e_i is the endothelial cell indicator function. The equations solved at each step of the algorithm are the following:

$$\frac{\partial v}{\partial t} = D_v \Delta v + b_v h_i (h - v^2/K_v) - k_0 v r_{v0} + k_{-0} r_v - \mu_v v, \quad (1)$$

$$\frac{\partial a_1}{\partial t} = b_{a1} e_i (p_i + h_i + n_i)(e_0 - a_1^2/K_a)$$
$$- k_1 a_1 r_{a0} + k_{-1} r_{a1} - \mu_{a1} a_1, \quad (2)$$

$$\frac{\partial a_2}{\partial t} = D_{a2}\Delta a_2 + b_{a2}e_i(p_i + h_i + n_i)(e_0 - a_2^2/K_a)$$

$$+ \bar{b}_{a2}h_i(h - a_2^2/K_a) - k_2a_2r_{a0} + k_{-2}r_{a2} - \mu_{a2}a_2, \quad (3)$$

$$\frac{\partial r_{v0}}{\partial t} = -k_0 v r_{v0} + k_{-0}r_v, \quad (4)$$

$$\frac{\partial r_{a0}}{\partial t} = -k_1 a_1 r_{a0} + k_{-1}r_{a1} - k_2 a_2 r_{a0} + k_{-2}r_{a2}, \quad (5)$$

$$\frac{\partial r_v}{\partial t} = k_0 v r_{v0} - k_{-0}r_v, \quad (6)$$

$$\frac{\partial r_{a1}}{\partial t} = k_1 a_1 r_{a0} - k_{-1}r_{a1}, \quad (7)$$

$$\frac{\partial r_{a2}}{\partial t} = k_2 a_2 r_{a0} - k_{-2}r_{a2}. \quad (8)$$

In these equations, $h(x,y,t)$ represents the concentration of hypoxic cells and e_0 represents the endothelial cell concentration per blood vessel. The system of differential equations contains 21 parameters, 13 of which were taken from experimental data. Parameters we were unable to find in the literature have been estimated. For more details on the parameter values, as well as information on the initial and boundary conditions and the numerical solver, the reader is referred to Ref. [14].

(b) *Vessel evolution*: check whether each vessel meets the requirements for regression or growth. Vessels with a concentration of bound Ang-2 six times greater than that of bound Ang-1 regress [33], provided that the concentration of bound VEGF is below its critical value. Vessel tips with a sufficient amount of bound VEGF sprout along the VEGF gradient.

(c) *Nonmalignant cells*: healthy cells undergo apoptosis if vessel regression causes its oxygen concentration to drop below a critical threshold (more particularly, if the distance of a healthy cell from a blood vessel exceeds the assumed diffusion length of oxygen, 250 μm [34]). Further, nonmalignant cells do not divide in the model. While nonmalignant cell division occurs in some organs, a hallmark of neoplastic growth is that tumor cells replicate significantly faster than the corresponding normal cells. Hence, we work under the simplifying assumption that nonmalignant division rates are so small compared to neoplastic division rates that they become relatively unimportant in the time scales we are considering. In the cases where this assumption does not hold, nonmalignant cellular division would have to be incorporated into the model.

(d) *Inert cells*: tumorous necrotic cells are inert. This assumption is certainly valid for the tumor type that motivated this modeling work, glioblastoma multiforme. In the case of glioblastoma, the presence of necrosis is an important diagnostic feature and, in fact, negatively correlates with patient prognosis [35].

(e) *Hypoxic cells*: a hypoxic cell turns proliferative if its oxygen level exceeds a specified threshold [14] and turns necrotic if the cell has survived under sustained hypoxia for a specified number of days. In the original algorithms, the transition from hypoxia to necrosis was based on an oxygen concentration threshold. However, given that cells (both tumorous and nonmalignant alike) have been shown to have a limited life span under sustained hypoxic conditions (without the oxygen concentration dropping below some critical threshold) [36], a temporal switch more accurately describes the hypoxic to necrotic transition. Thus, a novel aspect of the merged algorithm is a temporal hypoxic to necrotic transition. It has been measured that human tumor cells remain viable in hypoxic regions of a variety of xenografts for 4–10 days [36]. In our simulations, we will use the upper end of this measurement and assume that tumor cells can survive under sustained hypoxia for 10 days.

(f) *Proliferative cells*: a proliferative cell turns hypoxic if its oxygen level drops below a specified threshold. However, if the oxygen level is sufficiently high, the cell attempts to divide into the space of a viable nonmalignant cell in the growth-permitting region. The probability of division p_{div} is given by

$$p_{div} = p_0(1 - r/L_{max}), \quad (9)$$

where p_0 is the base probability of division, r is the distance of the dividing cell from the geometric center of the tumor, and L_{max} is the distance between the closest boundary cell in the direction of tumor growth and the tumor's center. In the original implementations of the algorithm, p_0 was fixed to be 0.192, giving a cell-doubling time of $\ln(2)/\ln(1+p_0)$ ≈ 4 days. In the merged algorithm proposed here, we wanted to account for fact that tumor cells with a higher oxygen concentration likely have a larger probability of dividing than those with a lower oxygen concentration. For this reason, we have modified the algorithm so that p_0 depends on the distance to the closest blood vessel d_{vessel} (which is proportional to the oxygen concentration at a given cell site). The average value of p_0 was fixed to be 0.192, and we have specified that p_0 takes on a minimum value p_{min} of 0.1 and a maximum value p_{max} of 0.284. This means that a proliferative cell in the model can have a cell doubling time anywhere in the range of 3–7 days. The formula used to determine p_0 is

$$p_0 = \frac{p_{min} - p_{max}}{D_{O_2}}d_{vessel} + p_{max}, \quad (10)$$

where D_{O_2} is the diffusion length of oxygen taken to be 250 μm [14]. Both p_{min} and p_{max} depend on the average probability of division. If this average probability changes, so does p_{min} and p_{max}.

(g) *Tumor center and area*: after each cell has evolved, recalculate the geometric center and area of the tumor.

From a strictly algorithmic perspective, some aspects of developing the merged model were fairly straightforward, for example, replacing one equation or algorithmic condition with another. Other aspects of developing the merged algorithm were more subtle. For example, developing a complete

vascular network using the random analog of the Krogh cylinder model and determining the combined vessel-boundary effect on cellular evolution involved more precisely defining the relationship between these interrelated tumor components as detailed above.

The merged algorithm demands a fairly large amount of computational resources. The storage of the Voronoi cell data, nearest-neighbor information, as well as vascular structure data requires a significant amount of memory. Solving the partial differential equations required to evolve the vasculature and determining the distance of a cell from the parametrized boundary require significant computational time. For these reasons, the merged algorithm has been developed in C++ and written in parallel using MPI. Using four nodes of Princeton's MaComp cluster (with 2 GB of memory and 2.2 GHz operating frequency) simulations over 5–6 months of simulated time take approximately 30 min.

B. Genetic mutations

In order to explain how we incorporated tumor cell heterogeneity into the merged algorithm, it is useful to state the assumptions under which we are working. We begin with the well-accepted supposition that tumors are monoclonal in origin; that is, a tumor mass arises from a single cell that accumulates genetic and epigenetic alterations over time [37]. Next, we suppose that as each tumor cell progresses through the cell cycle, there is a small probability that an error occurs in DNA replication. If the dividing cell is able to complete mitosis despite this error, the resulting mutation will be passed on to the cell's progeny. The mutation rate in nonmalignant human cells is very low and has been estimated to be between 10^{-7} and 10^{-6} mutations per gene per cell division [38]. Oftentimes, a phenotype found in cancer cells is the loss of DNA repair signaling. When this occurs, the mutation rate can be increased by a factor of $10^1 - 10^4$ [39]. In our model, we assume an average mutation rate of 10^{-6} in nonmalignant cells and that this rate is increased by a factor of 10^4 in cancerous cells giving a mutation rate of 0.01 mutations per cell division. The upper bounds were intentionally chosen to define the mutation rate, as the larger the mutation rate, the more opportunity we will have to study the emergence of mutant phenotypes in our model.

We are thus working under the assumption that there is a 1% chance a dividing cell will undergo a mutation in its genome. Provided that a mutation has occurred, we must define the potential phenotypes of mutant tumor cells. Given the tumor cell properties considered in the model, we will allow malignant cells to acquire altered phenotypes related to cell proliferation rates (the parameter p_0 defined previously) and the length of time a cell can survive under hypoxic conditions. While we do not need to explicitly consider the genetic mutations that can lead to these phenotypic changes, it is worth noting that each of the mutations considered in our automaton model can result from actual genetic alterations.

For example, the base proliferation rate of a cancer cell is related to its dependence on growth signals and antigrowth signals [1]. Tumor cells may increase their growth rate if they acquire the ability to secrete growth factors that mimic extracellular growth signals. Examples of this include tumor cells acquiring the ability to produce platelet-derived growth factor and tumor growth factor α [1]. Tumor cells can also increase their growth rate if they develop an insensitivity to antigrowth signals that typically cause the cell to arrest at the G1 or G2 phase of the cell cycle. A homozygous deletion in the RB gene that codes for pRb allows a cell to progress through the G1 phase of the cell cycle independent of DNA damage [1]. Similarly, a homozygous deletion in the TP53 tumor suppressor gene that codes for p53 allows damaged cells to progress through the G2 phase of the cell cycle independent of cell arrest signals [40]. Although we generally think of mutations benefiting a cancer cell (e.g., by increasing the base proliferation rate), it is also plausible that deleterious mutations can occur within a tumor cell. This is why we consider both kinds of mutations in our model.

A cell's ability to survive under sustained hypoxia also has a genetic component. The X-box binding protein 1 (XBP1) is known to undergo robust changes in gene expression during hypoxia [41]. Loss of XBP1 has been shown to increase the sensitivity of tumor cells to killing by hypoxia, and some tumor types overexpress XBP1 [41]. In our model, cells can acquire the ability to survive a longer-than-normal time period under hypoxia (corresponding to an overexpression of XBP1) and can acquire a deleterious mutation which decreases their life span under sustained hypoxia (corresponding to the underexpression of XBP1).

Given this background, we then "wire" each automaton cell in the algorithm with its own genome that encodes for the average base probability of division, p_0, and the lifetime of the cell under sustained hypoxia. In the current implementation of our model, a tumor cell expresses one of nine different phenotypes (eight being mutant phenotypes), all of which are defined in Fig. 1. The first generation of mutants (nodes following the first branch) corresponds to either an increase or decrease in the average base probability of division or in the amount of time a tumor cell can survive under sustained hypoxia. The second generation of mutants (the end nodes) corresponds to cells with mutations in both the average base probability of division and the amount of time a cell can survive under hypoxia. Each cell in the model divides with an error rate of 0.01 mutations per cell division. If a cell does mutate, it randomly chooses a phenotype in one of the nodes in the next level of the tree. In the absence of a mutation, daughter cells inherit the genome of the mother cell.

IV. RESULTS

The 2D cancer simulation tool presented herein has been used to study tumor growth in two confined environments: a 2D representation of the cranium and an irregularly shaped region. In the visualizations of the tumor which follow, we use the following convention: nonmalignant cells in the growth-permitting environment are white, the growth-prohibiting region is the white speckled region, nonmalignant cells that undergo apoptosis due to substandard oxygen levels in healthy tissue are green (intermediate gray shade if viewing in black and white), necrotic tumor cells are black,
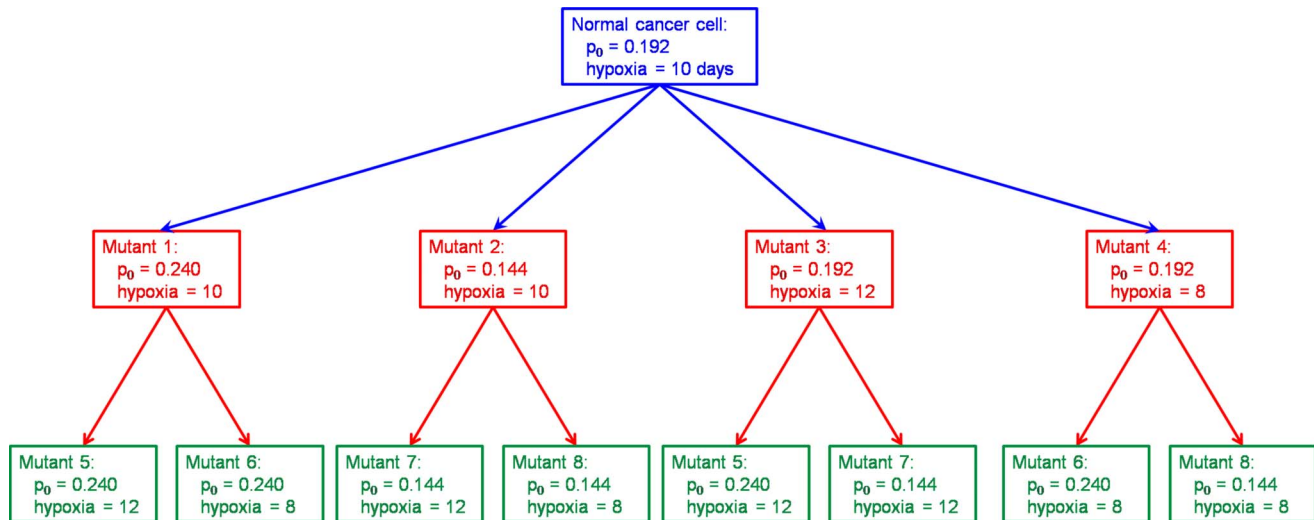
FIG. 1. (Color online) Tree illustrating potential mutant types that can derive from a specified parent cell. Root node contains the original tumor cell type, the nodes following the first branch contain all first-generation mutations, and the end nodes contain all second-generation mutations. Each type has a unique average base probability of division p_0 [which impacts both p_{min} and p_{max} as specified in Eq. (10) and the text that follows the equation] and a unique hypoxic life span (specified by the hypoxia parameter within each node of the tree).

hypoxic tumor cells are yellow (lightest gray shade if viewing in black and white), and proliferative tumor cells are a deep blue (darkest gray shade if viewing in black and white). Further, the lines running through the tumor and healthy tissue are blood vessels. If viewing in color, one can distinguish between those blood vessels that were originally part of the healthy capillary network (labeled red) as compared to those vessels that grew via angiogenesis (labeled purple).

In order to extract actual tumor length scales from the simulation units, one needs to consider both the size of the cells in an organ and the resolution of the algorithm (how many biological cells are represented by one automaton cell). For example, if we want to consider glioma growth in the brain, the average glial cell has a diameter of 40 μm [42]. If we assume that there is a one-to-one correspondence between a glial cell and an automaton cell (which is approximately 0.002 57 units in length our 2D simulations), then the entire region of space represented in the simulations would be 15.5×15.5 mm^2. The size of the region being considered is directly proportional to cell size. So, if we were to consider cells of a smaller size, or if we considered the fact that the effective shape of glial cells may be smaller than 40 μm due to their packing in the brain, the fixed grid considered here would correspond to a smaller region of tissue. Fortunately, this can be easily compensated for by increasing the number of cells in the underlying lattice. Another way to increase the size of the region considered is to incorporate more than one biological cell inside an automaton cell.

A. Simulating tumor growth

We begin by considering tumor growth in a 2D representation of the cranium. We treat the cranium as an elliptical growth-permitting environment with two growth-prohibiting circular obstacles representing the ventricular cavities. Tumor growth is initiated in between a ventricular cavity and

the cranium wall. In this setting, we find that the early-time characteristics of the tumor and the vasculature are not significantly different than those observed when radial symmetry is imposed on tumor growth [14]. In particular, after 45 days of growth [Fig. 2(a)], vessels associated with the radially symmetric tumor begin to regress and hypoxia results in the tumor center. 20 days later [Fig. 2(b)], a strong disordered angiogenic response has occurred in the still radially symmetric tumor. Over the next 50 days of growth [Figs. 2(c) and 2(d)], the disorganized angiogenic blood vessel network continues to vascularize the growing tumor, but the tumor's shape begins to deviate from that of a circle due to the presence of the confining boundary. The patterns of vascularization observed are consistent with the patterns observed in the original vascular model [14] suggesting that the merged algorithm maintains the functionality of the original vascular algorithm.

However, if we compare the results of this simulation with those of the environmentally constrained algorithm without the explicit incorporation of the vasculature [27] we find that the merged model seems to respond to the environmental constraints in a way that is more physically intuitive. In the original environmentally constrained algorithm [27], the tumor responds quickly and drastically to the confining boundary and ventricular cavities. This occurs because the original evolution rules not only determine the probability of division based on the distance to the boundary, but also determine the state of a cell based on a measure of its distance to the boundary. In the merged model which explicitly incorporates the vasculature, the state of each cell depends on the blood vessel network, and only the probability of division directly depends on the boundary. For this reason, the merged algorithm exhibits an emergent property in that it grows tumors that respond more gradually and naturally to environmental constraints than does the algorithm without the vasculature.
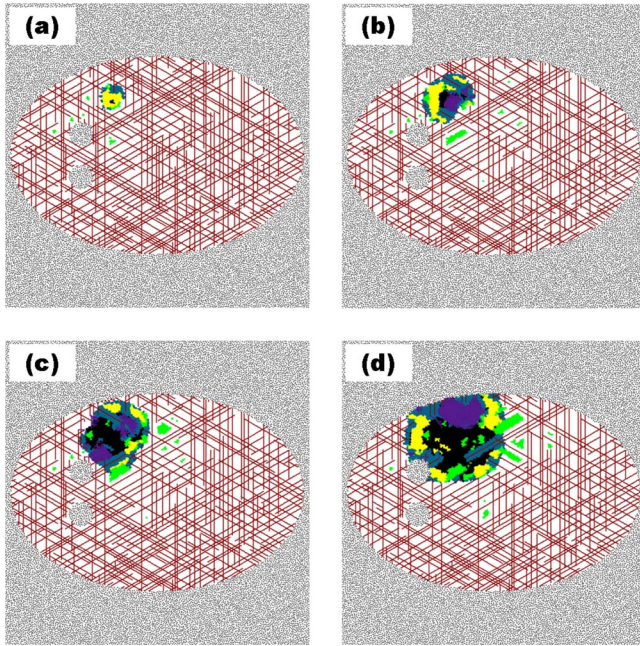
FIG. 2. (Color online) The temporal development of a tumor growing in a 2D representation of the cranium. (a) After 40 days, the dimensionless area is 0.0049 units^2, with 30% of the cells being proliferative, 66.4% being hypoxic, and 3.6% being necrotic. (b) After 65 days, the dimensionless area is 0.0195 units^2, with 51.2% of the cells being proliferative, 33.0% being hypoxic, and 15.8% being necrotic. (c) After 85 days, the dimensionless area is 0.0362 units^2, with 48.2% of the cells being proliferative, 16.8% being hypoxic, and 35.0% being necrotic. (d) After 115 days, the dimensionless area is 0.0716 units^2, with 45.1% of the cells being proliferative, 18.6% being hypoxic, and 36.3% being necrotic. The deep blue outer region (darkest of the grays in black and white) is comprised of proliferative cells, the yellow region (lightest of the grays in black and white) consists of hypoxic cells, and the black center contains necrotic cells. Green cells (intermediate gray shade in black and white) are apoptotic. The white speckled region of space represents locations in which the tumor cannot grow. The lines represent blood vessels. If viewing the image in color, red vessels were part of the original tissue vasculature and the purple vessels grew via angiogenesis.
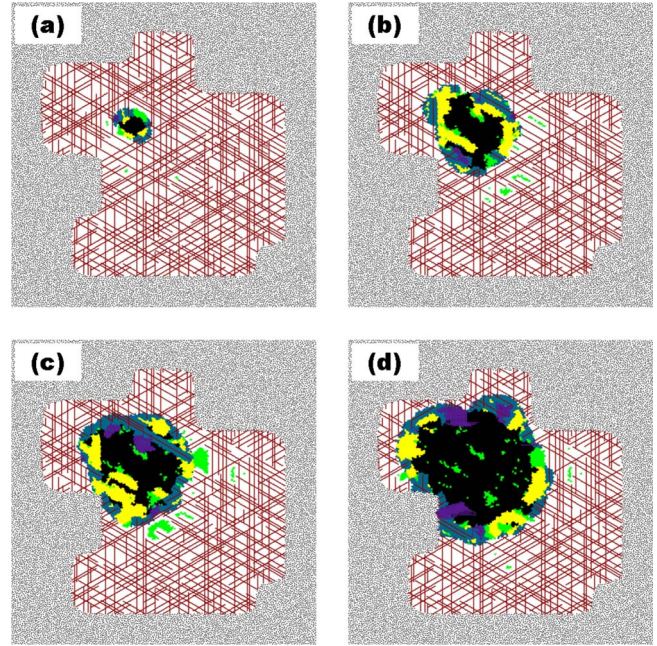
FIG. 3. (Color online) The temporal development of a tumor growing in an irregular asymmetric environment. (a) After 45 days, the dimensionless area is 0.0096 units^2, with 47.3% of the cells being proliferative, 8.9% being hypoxic, and 43.8% being necrotic. (b) After 100 days, the dimensionless area is 0.0644 units^2, with 30.9% of the cells being proliferative, 29.9% being hypoxic, and 39.2% being necrotic. (c) After 120 days, the dimensionless area is 0.1026 units^2, with 35.8% of the cells being proliferative, 23.7% being hypoxic, and 40.5% being necrotic. (d) After 165 days, the dimensionless area is 0.1694 units^2, with 25.3% of the cells being proliferative, 11.5% being hypoxic, and 63.2% being necrotic. The deep blue outer region (darkest of the grays in black and white) is comprised of proliferative cells, the yellow region (lightest of the grays in black and white) consists of hypoxic cells, and the black center contains necrotic cells. Green cells (intermediate gray shade in black and white) are apoptotic. The white speckled region of space represents locations in which the tumor cannot grow. The lines represent blood vessels. If viewing the image in color, red vessels were part of the original tissue vasculature and the purple vessels grew via angiogenesis.

The simulation of tumor growth in the 2D representation of the cranium does not quite capture that the merged algorithm truly allows the neoplasm to adapt its shape as it grows in a complex environment. This effect is not fully captured because the shape of the confining environment is rather simple in our representation of the cranium. There are certain regions in which tumors can grow that are structurally more complex and dynamic than what we have represented in Fig. 2. For instance, spinal cord tumors not only grow in a highly confined and irregularly shaped environment but are also subject to arbitrary if not continuous torsional movements of the neck and spine that further influence the shape of a developing neoplasm. Another example of a dynamic complex environment for tumor growth is the lungs. In this case, neoplasms can grow near the individual moving ribs of the chest and the periodic pressure imposed by the ribs can impact the shape and spread of a developing tumor [27].

While we currently do not consider such dynamic environments, we desire to present a study in which the growth-permitting region has a more irregular boundary than that of our 2D representation of the cranium. For this reason, we have designed an artificial growth environment with a highly irregular boundary (Fig. 3), and we have studied how and to what extent the shape of the tumor is altered by this environment. We find that for the first month and a half, the tumor grows in a radially symmetric fashion [Fig. 3(a)], as the confining boundary is not exerting any significant pressure on the tumor. This is consistent with the merged model retaining the functionality of the original confined growth algorithm. After three months of growth, the tumor slowly begins to adapt its shape in response to the mechanical confinement imposed by the region boundary [Figs. 3(b)–3(d)]. Just as with the 2D representation of the cranium, we notice an emergent property of the merged algorithm in that we find
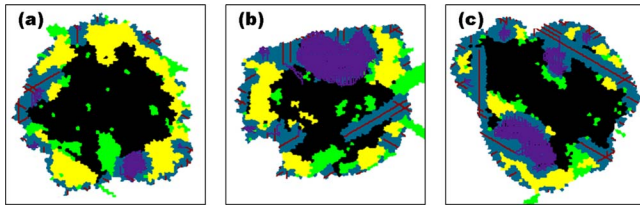
FIG. 4. (Color online) Snapshot of a simulated tumor taken out of its environment after approximately 4 months of growth. The tumors seen correspond to three different environments. (a) In the unbounded and homogeneous region, the tumor has a dimensionless area of 0.077 units^2 with 22.6% of the cells being proliferative, 26.4% being hypoxic, and 51.0% being necrotic. (b) In the 2D representation of the cranium, the tumor has a dimensionless area of 0.0716 units^2 with 45.1% of the cells being proliferative, 18.6% being hypoxic, and 36.3% being necrotic. (c) In the irregular region defined in Fig. 3, the tumor has a dimensionless area of 0.0812 units^2 with 45.9% of the cells being proliferative, 7.8% being hypoxic, and 46.3% being necrotic. The deep blue outer region (darkest of the grays in black and white) is comprised of proliferative cells, the yellow region (lightest of the grays in black and white) consists of hypoxic cells, and the black center contains necrotic cells. Green cells (intermediate gray shade in black and white) are apoptotic. The lines represent blood vessels. If viewing the image in color, red vessels were part of the original tissue vasculature and the purple vessels grew via angiogenesis.

that a more subtle and natural response to the effects of physical confinement occurs.

In order to pinpoint the effects that the aforementioned regions have on tumor growth, we will compare the shape and spread of a simulated tumor in these environments after approximately 4 months of growth to a tumor growing in an unbounded homogeneous region. In the unconfined region, the tumor is more or less circular after 4 months of growth [Fig. 4(a)]. The deviation from the circularity observed is actually a welcome result, as it is unexpected that a tumor would grow as a close-to-perfect circle *in vivo*, even in a symmetric environment. Both the structure of the vasculature and the stochasticity of the algorithm are responsible for these deviations from circularity. For both confined environments, the tumor remains more or less circular after 2 months of growth. [This data set is not shown, but in Figs. 2(a) and 3(a) the tumors can be seen after about a month and a half of growth.] Yet, in our 2D representation of the cranium, only 2 months after the tumor appears circular (after 4 months of growth), the neoplasms's shape has been significantly modified in response to the constraints imposed by the environment [Fig. 4(b)]. The indentation in the bottom left-hand corner of the tumor results from one of the ventricular cavities in the region, and the decrease in the tumor's curvature at its top end is due to the tumor's proximity relative to the confining cranium. Importantly, we note that it is possible for tumors to deform cavities. Since our algorithm does not account for this reciprocal deformation, it is plausible that the cavity's impact on the tumor shape is somewhat overestimated. Similarly, if we consider the tumor after 4 months of growth in the irregular region defined in Fig. 3, we observe that a bulbous structure has formed [Fig. 4(c)]. The narrowing of the tumor in its upper left-hand corner is a result of the

tumor growing through a tightly confined region of space. By taking each tumor out of the context of its environment and comparing it to a tumor which grew in an unbounded homogeneous region, we can pinpoint the changes induced in the tumor by each growth-permitting environment. An important conclusion drawn from the proposed simulation tool is that having an image of a tumor after some period of time is an insufficient amount of information if one seeks to properly deduce final tumor shape and size. At minimum, vascular structure and environmental boundaries must also be taken into account to accurately predict tumor growth dynamics.

A final note should be made about the images in the simulation. We have shown the tumor as a function of simulation time. Once a tumor has initiated aggressive growth, simulation time and actual time are a measure of the same quantity. However, the start of the simulation is not the same thing as the theoretical start of tumor growth. It often takes years for normal cells to undergo the phenotypic changes required to initiate aggressive tumor growth. Thus, while we have deadly tumor growth occurring on a 1 yr time scale in our simulations, this is actually 1 yr from the onset of aggressive growth, not 1 yr from the first mutations that eventually gives rise to the neoplastic cell population.

The results presented in this section need to be validated experimentally. While the individual pieces of this model have been validated, and while the model retains each tool's functionality, there are emergent properties and hence quantitative differences in the predictions being made by the merged algorithm. One way to validate the model would be to compare its predictions on the spatial composition of hypoxia to actual tumors. An array of techniques exist to measure hypoxic composition (see Ref. [43] for a critical review of such techniques), some of which can give spatial information on the presence of hypoxia within a tumor. Data such as this would go a long way to validate and/or suggest modifications that should be made to the present algorithm.

B. Emergence of genetic mutations

The proposed cancer simulation tool also allows one to account for the phenotypic heterogeneity found within a tumor mass. A large number of mutant phenotypes have been observed in cancer cells, and in this subsection we will focus on a simplified version of the problem in which cancer cells can acquire beneficial or deleterious mutations in one of two phenotypes. Besides being able to look at the growth dynamics of an individual tumor with a known genetic profile, the algorithm can also be used to predict the likelihood that different beneficial or deleterious mutations emerge at some point in the life of the tumor. We say that a subpopulation has emerged if at some point in the life of the tumor, the population comprises 10% or more of the proliferative and hypoxic cell population. The algorithm is run 100 times for 300 simulated days in order to examine the emergence of the mutant phenotypes defined previously. Table I gives the probability of emergence P of each individual phenotype, along with the confidence interval, which is given by

TABLE I. For each mutant phenotype, we present the probability of emergence (along with the confidence interval) and how likely it is for that mutation to occur *relative to* the likelihood that a neutral mutation occurs. Note that when we present the results for increased p_0, for example, we are looking at how many times this mutation occurred in isolation or with another mutation.

Mutation description	Probability of emergence	Odds of emergence (mutation:neutral)
Increased p_0	0.78 ± 0.041	2.108:1
Decreased p_0	0.07 ± 0.026	1:5.286
Longer hypoxic life span	0.28 ± 0.045	1:1.321
Shorter hypoxic life span	0.28 ± 0.045	1:1.321

$$\sqrt{\frac{P(1-P)}{\text{number of trials}}}. \qquad (11)$$

Table I also shows the odds that each beneficial or deleterious mutation emerges relative to a neutral mutation. A neutral mutation is a mutation that occurs in the genome but has no phenotypic effect at the cellular level; therefore, it can be thought of as the control variable in the simulations. It tells you the likelihood that a mutation with no effect emerges in the population. It is most useful to see how often a mutation emerges relative to this control case.

The first notable trend in Table I is that the malignant cells with an increased rate of proliferation tend to emerge in the tumor cell population, as would be expected. Although a mutant must occupy a rather large percent of the tumor population (10% or more) for us to consider that it has "emerged" in the model, we still find that the increased rate of proliferation mutation emerges in 78% of the simulations, which is more than twice as often as a neutral mutation. Although it is expected that beneficial mutations emerge in the tumor, it is certainly not intuitive that deleterious mutations will emerge in the population. Surprisingly, we found that the mutation which decreases the rate of proliferation emerges in 7% of the simulations. While this percent is not huge, the mutation is only approximately a 5:1 underdog as compared to a neutral mutation. This result suggests that deleterious mutations can emerge despite the fact that they confer no growth advantage to the tumor mass. A similar result has previously been found in Ref. [28].

Even more surprising results are found if we study the probability of emergence of malignant cells with an increased or decreased ability to survive under hypoxic conditions. From the perspective of the tumor mass, it is most beneficial for the tumor cells to survive as long as possible under hypoxic conditions. This way, if the angiogenic vasculature lags behind the growth of the tumor, a larger number of cells can persist in a hypoxic state until the vasculature "catches up" to the tumor size. However, we found that mutations which lengthen or shorten a cell's hypoxic life span by 20% are equally likely to emerge.

It seemed surprising that increasing survival under hypoxia was not selected for over a neutral mutation. It was also surprising that there was no difference in emergence when increasing or decreasing the survival time under hypoxia. For these reasons, we decided to test how larger variations in the hypoxic life span impact the emergence of the mutation. We found that the mutation which decreases the hypoxic life span to 4 days emerges in 21% (1:1.762) of the tumors, whereas the mutation that increases the hypoxic life span to 16 days emerges in 57% (1.54:1) of the tumors. Thus, a more significant decrease in the hypoxic life span emerges less frequently than a neutral mutation, although this phenotype emerges in a significant percent of the tumors. Further, a large increase in the hypoxic life span is selected for in the tumor population, as it emerges more frequently than a neutral mutation.

The results concerning mutation emergence are in need of experimental validation. For example, focusing our attention on hypoxic life span, is having a hypoxic life span slightly above or below the average equally represented in the tumor population, as our simulations predict? Are more significant increases in the hypoxic life span found more commonly than more significant decreases? Also, are there different temporal patterns of mutation emergence in real tumors? Although we did not explore this fully in our model, the model can also track the likelihood of a tumor expressing different mutations in a temporal manner. With experimental data on the prevalence and importance of this sort of mutation, the model can be utilized to better understand the effects this mutation has on tumor growth and response to treatment.

V. DISCUSSION

The cancer simulation tool that is presented in this paper is able to account for the heterogeneous nature of a tumor and its environment, and how interactions between these environments impact neoplastic progression. To demonstrate the utility of the class of models we have developed, we describe what we have learned about some necessary, although not sufficient, features that must be included in any clinically relevant *in silico* model of tumor growth. In particular:

(1) Without incorporating environmental confinement effects, tumor size, shape, and spread cannot be properly predicted even if we are given an image of the tumor at a fixed point in time. This was illustrated in Fig. 4, where all masses started as circular tumors, but the future shape of the masses diverged as time progressed.

(2) Only by including the vasculature with physical confinement effects can more subtle changes in tumor shape be captured, as was discussed in Sec. IV. The vasculature, however, need not be present for accurately capturing approximate growth dynamics, provided the tumor is known to be in the "macroscopic growth regime" (that is, the tumor has the ability to initiate angiogenesis) [14].

(3) The vasculature does need to be incorporated, however, if we want to consider the initial growth conditions required for a tumor to grow to a clinically relevant size, and if we want to test treatment strategies that target tumor-associated blood vessels. This was demonstrated in significant detail in Ref. [14].

(4) Failure to account for a tumor's genetic (really, phenotypic) profile can lead to markedly inaccurate predictions

on tumor shape and size. This was demonstrated in more detail in Ref. [28].

In this paper, we have demonstrated the ability of the merged algorithm to predict tumor size, shape, and spread as a function of time along with its ability to qualitatively track the evolution of the vasculature and to incorporate genetic mutations. As a next step, we hope to calibrate the model with patient-specific data, with the long-term goal of using the model in clinical applications.

There is work that can be done to improve upon the merged model of tumor growth presented here. First and foremost, we would like to develop a more realistic representation of the capillary network. While visually our model of the vasculature may contradict some expectations, it is important to recognize that we are not trying to model a vascular tree that branches from the arteries to the arterioles into the capillaries, and from the capillaries to the venules and veins. Instead, we are only considering the level of the vascular tree at which oxygen and nutrient exchange occurs, i.e., the capillary level. Thus, while at first glance our vascular model does not look ideal, and while there is room for improvement, it is important to remember that we are only concerning ourselves with the capillary network, which does not exhibit the same branching structure as is seen in higher-order vessels. There is one other issue that arises as a result of our representation of the capillary network. The individual line segments that are laid down in the model to represent the capillaries are rather long. As a result, when a blood vessel regresses, this regression can affect cells that are significantly far from the tumor (see Figs. 2 and 3). This extratumoral apoptosis, especially at far distances from the tumor, is an artifact of an inaccurate representation of the capillary network and is not something we hypothesize would be found in real tissues. This is not to say that there may not be apoptosis in areas that immediately surround the tumor, but one would not expect apoptosis significantly far from the tumor.

For these reasons, in future work, we do intend on improving upon the capillary network utilized in our model. However, instead of developing a new model at the 2D level, it is essential that we develop a 3D model of the capillary network in order to simulate volumetric tumor growth. Thus, improvements upon the current model pivot upon developing a new 3D model of the capillary network and generalizing the automaton rules to work in 3D space. It is interesting to note, however, that recent work has shown that if the same growth mechanisms are applied in 2D and 3D, 2D results can be mapped onto 3D results [22]. This may allow us to avoid the computational difficulties of generalizing the algorithm to 3D.

Another improvement that can be made on the algorithm concerns the current treatment of physical obstacles to tumor growth as rigid boundaries. Medical imaging technologies, including magnetic resonance imaging (MRI) and computed tomography (CT) scans can readily provide information on the presence of anatomical boundaries, although these images do not give information on the deformable nature of these boundaries. This is the reason we chose to use rigid boundaries in the model, although it is not necessarily the case that all obstacles to tumor growth are rigid structures.

The deformable nature of anatomical structures was accounted for in work done by Sansone *et al.* [44]. In particular, the effects of pressure from anatomical constraints against a growing tumor were accounted for by looking at the hardness of different tissues [44]. While we looked at boundary effects on mass growth, boundaries also have effects on other biophysical properties of cells including cell-to-cell aggregation. Given that our tumor cells are discretely represented on a fixed grid, we are unable to take such effects into account. However, it is important to note that the effects of boundaries on cell-to-cell aggregation and cell survival probabilities have been studied by others [45,46]. Our model could benefit from incorporating deformable boundaries and other biophysical effects of these boundaries in the future.

There are certainly many other features of tumor growth, including some forms of tumor-host interactions, that may be necessary to include in a cancer simulation tool with clinical applications. For example, a cancer can alter the surrounding extracellular matrix and can modify the immune system as it develops [2]. A number of models have accounted for these other forms of tumor-host interactions [4,7–9,15]. It is worthy of future investigation to determine how these other cancer models can be incorporated into our merged model. This process can be as easy as putting two models on one computational grid, or it can be much more complex and involve significant theoretical changes to both models.

Finally, cancer cells can break off the main tumor mass and invade healthy tissue. For certain tissue types, this process can eventually result in metastases in other organs. A cancer in which invasion, although not metastasis, must be considered in an effort to understand tumor dynamics is glioblastoma multiforme. Glioblatoma is a cancer that arises from the glial cells or their precursors in the central nervous system [47]. Tumor-cell invasion is a hallmark of glioblastomas, as individual tumor cells have been observed to spread diffusely over long distances and can migrate into regions of the brain essential for the survival of the patient [47]. While MRI scans can recognize mass tumor lesions, these scans are not sensitive enough to identify malignant cells that have spread well beyond the tumor margin [48]. Thus, understanding the distribution of these invasive cells in the brain is essential for having a simulation tool for glioblastoma that is useful in a clinical setting. Similarly, for other tumor types, the metastatic process is essential in understanding tumor recurrence, and hence patient prognosis. In future work, we hope to extend the merged model to address the impacts that the tumor microenvironment [49], tumor vasculature, cell-to-cell adhesion, and long-range cell signaling [50] have on single-cell invasion, metastasis, and response to treatment. In particular, recent mathematical models [51,52] have demonstrated that the invasive phenotype of tumor cells is favored in the presence of a heterogeneous distribution of oxygen and nutrients, while suppressed in the presence of a homogeneous oxygen distribution. Using information on cellular phenotype, oxygen distribution, and environmental confinement, we can modify our model to be able to track the invasion of cells along the blood vessels and into the healthy tissue. By incorporating invasion, other types of interactions into our model, we can determine a larger list of necessary

conditions to include in a clinically relevant cancer simulation tool. A long-term goal is to develop a sufficient list of such conditions; that is, a list of features that, if incorporated into a simulation tool, would be sufficient to predict neoplastic growth and response to treatment.

Just as would be required for a clinically relevant simulation tool, the algorithm proposed here can probe the effects that different therapeutic strategies have on tumor survival. Since much of the biological detail in the model relates to the vasculature, the model can be used to study the impact that vascular-targeting therapies have on tumor growth. In the future, we plan to explore tumor response to different angiogenic-inhibitors and vascular-disrupting agents administered in isolation or in combination with a standard anti-growth agent. We expect the model to make many predictions that can be tested experimentally. For example, if we identify a novel drug target or a combination of drugs, experiments can be done to test the drugs effects *in vivo*. On the other hand, if the model suggests a reason that a certain therapeutic route is unsuccessful, targeted experiments can be done to test the validity of such predictions. The results of such experiments would then feed back into the model allowing the model to grow in both scope and accuracy. In the future, we aim to have a simulation tool that can be utilized in the clinic to predict tumor growth and guide treatment strategies.

VI. CONCLUSIONS

We have merged, adapted, and improved on individual models of tumor growth [14,21,27,28], each of which were successful at achieving their individual goals, into a more comprehensive cancer simulation tool. The current CA model accounts for angiogenesis, physical confinement and environmental heterogeneity, and genetic mutations. We not only presented the algorithmic development of the tool, but we also utilized the tool to predict tumor progression in several confined vascular environments. Furthermore, we demonstrated that the tool can be utilized to develop a list of necessary features to incorporate in a cancer simulation tool with clinical applications. Although there are many more processes to be considered, the algorithm presented here represents the first time our tumor-modeling efforts have been brought together into one algorithm with the potential to address a variety of questions about neoplastic growth and survival. In the future, we anticipate this model be expanded upon by both ourselves and others to incorporate a wider range of processes that contribute to tumor development and expansion. We also plan to further exploit the model by testing new sets of questions including but not limited to how the genetic profile of a tumor influences its response to a combination of cytotoxic and vascular-targeting drugs and how drug delivery to a tumor mass is influenced by a confining environment. We expect our theoretical explorations to lead to questions that can be tested experimentally. As a long-term goal, we hope that this back-and-forth interaction between biologists and theoreticians will eventually lead to the development of a cancer simulation tool powerful enough to be utilized in the clinic.

Ultimately, any comprehensive tumor model must be able to account for tumor mechanisms across many length scales. There are a variety of levels of complexity that can be further added to the present model. For example, allowing for a more microscopic description of tissue structure [49] and physical properties is crucial. For this purpose, one can exploit advances in the theory of heterogeneous materials that enable one to predict transport and mechanical properties from the microstructure [32,53,54]. As an example, the theory of random heterogeneous materials enables the characterization of diffusion and flow through complex media [32]. Therefore, questions related to the diffusion of a drug through a tumor, the transport of oxygen and waste into and out of the tumor, the flow of blood through the tumor vasculature, or the invasion of cancer cells into healthy tissue could benefit by applying techniques from the field of random heterogeneous materials.

[1] D. Hanahan and R. A. Weinberg, Cell **100**, 57 (2000).

[2] H. Kitano, Nat. Rev. Cancer **4**, 227 (2004).

[3] T. S. Deisboeck, M. E. Berens, A. R. Kansal, S. Torquato, A. Rachamimov, D. N. Louis, and E. A. Chiocca, Cell Prolif. **34**, 115 (2001).

[4] T. Alarcón, H. M. Byrne, and P. K. Maini, Multiscale Model. Simul. **3**, 440 (2005).

[5] A. Bankhead III and R. B. Heckendorn, Genet. Program. Evolvable Mach. **8**, 381 (2007).

[6] S. L. Spencer, R. A. Gerety, K. J. Pienta, and S. Forrest, PLOS Comput. Biol. **2**, e108 (2006).

[7] R. A. Gatenby, Eur. J. Cancer **32**, 722 (1996).

[8] N. Bellomo and L. Preziosi, Math. Comput. Model. **32**, 413 (2000).

[9] L. G. de Pillis, A. E. Radunskaya, and C. L. Wiseman, Cancer Res. **65**, 7950 (2005).

[10] M. Scalerandi, B. C. Sansone, and C. A. Condat, Phys. Rev. E **65**, 011902 (2001).

[11] M. Scalerandi and B. C. Sansone, Phys. Rev. Lett. **89**, 218101 (2002).

[12] B. Capogrosso Sansone, C. A. Condat, and M. Scalerandi, Eur. Phys. J. Appl. Phys. **25**, 133 (2004).

[13] M. Scalerandi and M. Griffa, Phys. Scr. T **118**, 179 (2005).

[14] J. L. Gevertz and S. Torquato, J. Theor. Biol. **243**, 517 (2006).

[15] M. L. Martins, S. C. Ferreira, Jr., and M. J. Vilela, Phys. Life Rev. **4**, 128 (2007).

[16] R. H. Thomlinson and L. H. Gray, Br. J. Cancer **9**, 539 (1955).

[17] A. C. Burton, Growth **30**, 157 (1966).

[18] R. P. Araujo and D. L. S. McElwain, Bull. Math. Biol. **66**, 1039 (2004).

[19] V. Cristini, J. Lowengrub, and Q. Nie, J. Math. Biol. **46**, 191 (2003).

[20] A. M. Stein, T. Demuth, D. Mobley, and M. Berens, Biophys. J. **92**, 356 (2007).

[21] A. R. Kansal, S. Torquato, R. G. Harsh IV, E. A. Chiocca, and T. S. Deisboeck, J. Theor. Biol. **203**, 367 (2000).

[22] M. Radszuweit, M. Block, J. G. Hengstler, E. Schöll, and D. Drasdo, Phys. Rev. E **79**, 051907 (2009).

[23] R. Lev Bar-Or, R. Maya, L. A. Segel, U. Alon, A. J. Levine, and M. Oren, Proc. Natl. Acad. Sci. U.S.A. **97**, 11250 (2000).

[24] K.-H. Cho, S.-Y. Shin, H.-W. Lee, and O. Wolkenhauer, Genome Res. **13**, 2413 (2003).

[25] A. R. Asthagiri and D. A. Lauffenburger, Biotechnol. Prog. **17**, 227 (2001).

[26] C. V. Rao, D. M. Wolf, and A. Arkin, Nature (London) **420**, 231 (2002).

[27] J. L. Gevertz, G. Gillies, and S. Torquato, Phys. Biol. **5**, 036010 (2008).

[28] A. R. Kansal, S. Torquato, E. A. Chiocca, and T. S. Deisboeck, J. Theor. Biol. **207**, 431 (2000).

[29] J. E. Schmitz, A. R. Kansal, and S. Torquato, J. Theor. Med. **4**, 223 (2002).

[30] J. Holash, P. C. Maisonpierre, D. Compton, P. Boland, C. R. Alexander, D. Zagzag, G. D. Yancopoulos, and S. J. Weigand, Science **284**, 1994 (1999).

[31] G. Helmlinger, P. A. Netti, H. C. Lichtenbeld, R. Melder, and R. K. Jain, Nat. Biotechnol. **15**, 778 (1997).

[32] S. Torquato, *Random Heterogeneous Materials: Microstructure and Macroscopic Properties* (Springer-Verlag, New York, 2002).

[33] C. S. Maisonpierre *et al.*, Science **277**, 55 (1997).

[34] X. Zheng, S. M. Wise, and V. Cristini, Bull. Math. Biol. **67**, 211 (2005).

[35] S. M. Raza, F. F. Lang, B. B. Aggarwal, G. N. Fuller, D. M. Wildrick, and R. Sawaya, Neurosurgery **51**, 2 (2002).

[36] R. E. Durand and E. Sham, Int. J. Radiat. Oncol., Biol., Phys. **42**, 711 (1998).

[37] P. J. Fialkow, Annu. Rev. Med. **30**, 135 (1979).

[38] A. L. Jackson and L. A. Loeb, Genetics **148**, 1483 (1998).

[39] I. P. M. Tomlinson, M. R. Novelli, and W. F. Bodmer, Proc. Natl. Acad. Sci. U.S.A. **93**, 14800 (1996).

[40] W. R. Taylor and G. R. Stark, Oncogene **20**, 1803 (2001).

[41] L. Romero-Ramirez *et al.*, Cancer Res. **64**, 5943 (2004).

[42] W. C. Broaddus, P. J. Haar, and G. T. Gillies, *Encyclopedia of Biomaterials and Biomedical Engineering* (Dekker, New York, 2004).

[43] S. Davda and T. Bezabeh, Cancer Metastasis Rev. **25**, 469 (2006).

[44] B. Capogrosso Sansone, P. P. Delsanto, M. Magnano, and M. Scalerandi, Phys. Rev. E **64**, 021903 (2001).

[45] J. Galle, M. Hoffman, and G. Aust, J. Math. Biol. **58**, 261 (2009).

[46] K. Puskar, S. Ta'asan, R. Schwartz, and P. R. LeDuc, Cell Biochem. Biophys. **45**, 195 (2006).

[47] E. C. Holland, Proc. Natl. Acad. Sci. U.S.A. **97**, 6242 (2000).

[48] T. Visted, P. O. Enger, M. Lund-Johansen, and R. Bjerkvig, Front. Biosci. **8**, e289 (2003).

[49] J. L. Gevertz and S. Torquato, PLOS Comput. Biol. **4**, e1000152 (2008).

[50] A. R. Kansal and S. Torquato, Physica A **301**, 601 (2001).

[51] V. Cristini, H. B. Frieboes, R. Gatenby, S. Caerta, M. Ferrari, and J. Sinek, Clin. Cancer Res. **11**, 6772 (2005).

[52] H. B. Frieboes, X. Zheng, C.-H. Sun, B. Tromberg, R. Gatenby, and V. Cristini, Cancer Res. **66**, 1597 (2006).

[53] I. C. Kim and S. Torquato, J. Appl. Phys. **69**, 2280 (1991).

[54] S. Torquato, Int. J. Solids Struct. **37**, 411 (2000).